Available online at www.sciencedirect.com
ScienceDirect
Planetary and Space Science 56 (2008) 1506–1516
Planetary and Space Science
www.elsevier.com/locate/pss

On the impact of multiply charged heavy solar wind ions on the surface of Mercury, the Moon and Ceres

E. Kallio[a,*], P. Wurz[b], R. Killen[c], S. McKenna-Lawlor[d], A. Milillo[e], A. Mura[e], S. Massetti[e], S. Orsini[e], H. Lammer[f], P. Janhunen[a], W.-H. Ip[g]

[a]*Finnish Meteorological Institute, Erik Palmenin aukio 1, P.O. Box 503, Helsinki 00101, Finland*
[b]*University of Bern, Physikalisches Institut, CH-3012 Bern, Switzerland*
[c]*Department of Astronomy, University of Maryland, College Park, MD 20742, USA*
[d]*Space Technology Ireland, National University of Ireland, Maynooth, Co. Kildare, Ireland*
[e]*Instituto di Fisica dello Spazio Interplanetari, I-00133 Rome, Italy*
[f]*Space Research Institute, Austrian Academy of Sciences, Schmiedlstr. 6, 8042 Graz, Austria*
[g]*Institute of Astronomy, National Central University, Central University Road, 32054 Chung-Li, Taiwan*

Received 12 January 2008; received in revised form 2 July 2008; accepted 16 July 2008
Available online 30 July 2008

Abstract

We have studied the impact of multiply charged solar wind O^{7+} and Fe^{9+} ions on the surfaces of Mercury, the Moon and on a Ceres-size asteroid using a quasi-neutral hybrid model.

The simulations showed that heavy O^{7+} and Fe^{9+} ions impact on the surface of Mercury non-homogenously, the highest flux being near the magnetic cusps—much as in the case of impacting solar wind protons. However, in contrast to protons, the analyzed heavy ions do not create high ion impact flux regions near the open–closed magnetic field line boundary. Dawn–dusk asymmetry and the total ion impact flux were each found to increase with respect to the increasing mass per charge ratio for ions, suggesting that the Hermean magnetic field acts as a mass spectrometer for solar wind ions. The Moon, in contrast, does not have a global intrinsic magnetic field and, therefore, solar wind ions can freely impact on its surface when this body is in the solar wind. The same is true for a, non-magnetized, Ceres-size asteroid.

The impact of multiply charged ions on a solid surface results in a large variety of physical processes, of often intimately inter-related atomic reactions, e.g. electron exchange between solid and approaching projectile, inelastic scattering of projectile, electronic excitation in the projectile and/or the solid, ejection of electrons, photons, neutral and iodized surface particles, and eventual slowing down and stopping of the projectile in the solid. The electron transfer process between impacting heavy ions and surface constituents can result in soft X-ray ($E<1$ keV) and extreme ultraviolet (EUV) photon emissions. These processes will eventually damage the target surface. Analysis of the hybrid Mercury model (HYB-Mercury) suggests that, at this planet the damaging processes result in non-homogenous ageing of the surface that is controlled by the intrinsic magnetic field of the planet and by the direction of the interplanetary magnetic field. In the corresponding Lunar model (HYB-Moon) and in the non-magnetized asteroid model (HYB-Ceres), surface ageing is demonstrated to take place on that side of the body that faces toward the flow of the solar wind.

Keywords: Mercury; The Moon; Ceres; Multiply charged heavy solar wind ions; Plasma–surface interaction; Numerical simulation

1. Introduction

Mercury is a planet with a relatively weak intrinsic magnetic field, and without an atmosphere. The Moon, instead, has neither an atmosphere nor a global intrinsic magnetic field. Many non-magnetized and non-atmospheric objects with sizes smaller than the Moon are found in the asteroid belt between the orbit of Mars and Jupiter as well as beyond Neptune (the Trans-Neptunian objects). The surfaces of these objects are, therefore, subject to bombardment by impacting solar wind ions: protons (H^+),

*Corresponding author. Tel.: +358 9 1929 4636.
E-mail address: Esa.Kallio@fmi.fi (E. Kallio).

0032-0633/$ - see front matter © 2008 Elsevier Ltd. All rights reserved.
doi:10.1016/j.pss.2008.07.018

alpha particles (He^{++}) and multiply charged heavy ions (O^{6+}, O^{7+}, Fe^{9+}, C^{4+}, Ne^{8+}, etc.).

Ion impact on the surface of an obstacle is a manifestation of a direct plasma–surface interaction and it has many potential consequences with regard to the surface (e.g. Killen and Ip, 1999; Milillo et al., 2005; Wurz et al., 2007). For example, impacting ions can dislodge neutrals, ions and electrons from the surface, thereby affecting both the surface itself and its plasma and neutral atom environments.

The impact of solar wind protons on the surface of Mercury has already received considerable attention in the literature. In these studies the properties of the impacting solar wind protons were based on global, modified terrestrial magnetospheric models which had been adapted to Hermean conditions (Killen et al., 2001; Delcourt et al., 2002; Wurz and Lammer, 2003; Massetti et al., 2003; Mura et al., 2005; Sarantos et al., 2007) and a self-consistent quasi-neutral hybrid model (Kallio and Janhunen, 2003a, b) was also presented. The interaction of solar wind ions (protons and alpha particles) with the Moon has been investigated recently (Wurz et al., 2007).

However, a fraction of the impacting solar wind plasma contains also multiply charged solar wind ions, such as O^{6+}, O^{7+}, Fe^{9+} to Fe^{14+}, C^{4+}, C^{5+}, Ne^{8+}, etc. (see, for example, von Steiger et al., 2000, and references therein). From sputter experiments in the laboratory it is known that the potential energy which is stored in multiply charged ions is liberated when the ions recombine during impacts on solid surfaces (Aumayr and Winter, 2003). In addition to their kinetic energy, the potential energy carried by multiply charged ions can lead to a kind of ion-induced sputtering which is called potential sputtering. Furthermore, the interaction between multiply charged ions and neutral species originating from a solar system object can result in a charge exchange (CX) process where an ion captures an electron from a neutral atom or molecule. In case of a significant atmosphere the CX processes cause the soft X-ray emission, as was observed from comets (Cravens, 1997, 2002). Soft X-ray and extreme ultraviolet (EUV) photon emission is also anticipated to take place in planetary exospheres, such as at the Earth (Robertson and Cravens, 2003), Mars (Holmström et al., 2001) and Venus (Gunell et al., 2007). For the objects considered in this paper, which have no atmosphere and only a thin exosphere, the multiply charged ions will interact with the material of the surface.

There is a considerably large body of laboratory research on the interaction of multiply charged ions with solid surfaces, which has been reviewed recently for multiply charged ions (Arnau et al., 1997; Aumayr and Winter, 2003), and for highly charged ions (Schenkel et al., 1999). However, possible effects of impacting multiply charged solar wind ions on the surface of solar system objects has received little attention hitherto. One reason for this is the lack of laboratory experiments and numerical simulations that could describe the complicated processes associated with different projectiles and targets. Recently, it was suggested (Shemansky, 2003) that impacting, multiply charged, solar wind ions results in soft-X-ray emission that produces ionization and dissociation of the molecular structure of relevant surfaces, resulting in even more effective ion sputtering than is caused by impacting solar wind protons. On the other hand, it was also recently concluded, based on available laboratory data, that a significant increase in the sputter yield due to impacting multiply charged ions cannot be expected at planetary surfaces (Wurz et al., 2007).

For this paper, we calculated the flux of impacting solar wind O^{7+} ions on three solar system objects using a self-consistent, quasi-neutral, hybrid model. The three objects are (1) Mercury which has a magnetosphere due to its relatively weak intrinsic magnetic field, (2) the non-magnetized Moon when it is in the solar wind and (3) a Ceres-size asteroid, assuming that this has a negligible intrinsic magnetic field and is without an atmosphere. The role of the mass per charge ratio of the heavy impacting ions at Mercury is also studied through calculating the impacting flux of solar wind Fe^{9+} ions.

The paper is organized as follows. First, we describe the numerical model adopted and give an overview of the solar wind interaction with three objects of different sizes at different distances from the Sun. Then we present the fluxes of impacting H^+, O^{7+} and Fe^{9+} ions on the surface of Mercury and compare these with ion impacts on the Moon and on an asteroid. Finally, we address issues involving effects resulting from CX processes near the surfaces of the three objects.

2. Description of the HYB models

The ion impact flux was calculated using a self-consistent, three-dimensional (3D), quasi-neutral hybrid model. In a quasi-neutral hybrid model, or briefly in a hybrid model, ions are modelled as particles while electrons form a massless charge neutralizing fluid. An important feature in the hybrid model simulation is that ions can impact to the surface of the object, making it possible to study the flux of impacting ions at a given position on the surface of the object considered. Our Mercury hybrid model (which is called HYB-Mercury), and the hybrid Moon model (which is called HYB-Moon) are described in detail elsewhere (Kallio and Janhunen, 2003a, b; Kallio, 2005) and we describe here only those features that are of special importance for the present study.

In all three runs of the model, the coordinate system was such that the solar wind flowed in the $-x$-direction, $+z$-axis was perpendicular to the orbital plane of the object and $+y$-axis completed the right-hand system. The centre of the object was at the origin at $(x,y,z) = (0,0,0)$.

In the HYB-Mercury model, the Hermean intrinsic magnetic field was modelled as a magnetic dipole located at the centre of the planet. The magnetic moment was on the z-axis and the magnetic field on the surface of Mercury at

$r = 1R_M$ at the magnetic equator ($z = 0$) was $[B_x, B_y, B_z] = [0, 0, 300]$ nT (here $r = (x^2+y^2+z^2)^{1/2}$ and $R_M = 2440$ km is the radius of Mercury adopted in the simulation). The ions were collected during 35–50 s time intervals starting at 180 s from the beginning of the simulation. In the HYB-Mercury model, the upstream values were run as before for the so-called pure northward IMF case (Kallio and Janhunen, 2003a, b) where the density of the solar wind protons, $n_{SW}(H^+)$ was taken to be 72 cm^{-3}, the velocity of the solar wind protons, $\boldsymbol{U}_{SW}(H^+) = [U_x, U_y, U_z]$ was $[-430,0,0]$ km s^{-1}, and the interplanetary magnetic field, $\boldsymbol{B}_{SW} = [B_x, B_y, B_z]$ was [0,0,10] nT.

In the HYB-Moon model the upstream parameters corresponded to the nominal solar parameters at one astronomical unit (AU) where $n_{SW}(H^+) = 6\,cm^{-3}$, $\boldsymbol{U}_{SW}(H^+) = [-430, 0, 0]$ km s^{-1} and $\boldsymbol{B}_{SW} = 7\,nT \times [\cos(45^\circ), \sin(45^\circ), 0] = [7, 7, 0] \times 2^{-1/2}$ nT. The radius of the Moon used in the simulation was 1730 km and the Moon was modelled as a non-magnetized insulator.

The HYB-Ceres model is similar to the HYB-Moon model except that the radius of the obstacle is assumed to be 470 km (the radius of asteroid Ceres). In the HYB-Ceres model the upstream conditions mimicked the solar wind plasma parameters at the position of Ceres at ~2.9 AU, namely $n_{SW}(H^+) = 0.86\,cm^{-3}$, $\boldsymbol{U}_{SW}(H^+) = [-430, 0,0]$ km s^{-1}. When Ceres is at 2.9 AU the Parker spiral angle is about 70°. However, in this paper, the IMF was assumed, for simplicity, to be perpendicular to the flow with $\boldsymbol{B}_{SW} = [0, 0.83, 0]$ nT. In all three models the thermal velocity was taken to be 10% of the solar wind bulk velocity.

The ion impact simulations were performed as follows. The size of the simulation box in HYB-Mercury model in the x-direction (L_x), in the y-direction (L_y), and in the z-direction (L_z), was $[-4, 4]R_M$. The size of the grid, ΔL, was 305 km and the average number of ions within a grid cell, n_{ave}, was 20. The total number of ions, N_{tot}, was about 5.4×10^6. In the HYB-Moon run the numerical simulation parameters were $L_x = [-3.8, 1.8]R_L$ ($R_L = 1730$ km was the Lunar radius used in the simulation), $L_y = L_z = [-2.8, 2.8]R_L$, $\Delta L = 173$ km, $n_{ave} = 30$, and $N_{tot} = 3.8 \times 10^6$. In the HYB-Ceres model $L_x = [-9.4, 1.8]R_C$ ($R_C = 470$ km was the radius of Ceres in the simulation), $L_y = L_z = [-4.2, 4.2]R_C$, $\Delta L = 47$ km, $n_{ave} = 10$, and $N_{tot} = 8.6 \times 10^6$.

The new feature of the runs analyzed in this study compared with our earlier Mercury and Moon simulations is that the solar wind is assumed to include 0.07% (7×10^{-4}) of multiply charged, heavy solar wind oxygen O^{7+} ions, that is the solar wind is taken to have an oxygen ion population with particle density $n_{SW}(O^{7+}) = 7 \times 10^{-4} \times n_{SW}(H^+)$. Bame et al. (1975) reported for the oxygen abundance in the solar wind $[H/O] = 1900 \pm 400$. The O^{7+} ion is one of the few charge states of oxygen ions in the solar wind, which range from about O^{5+} to O^{8+}, with the O^{7+} fraction typically being 0.25, the O^{6+} fraction about 0.75, and the other charge states being much less abundant for regular solar wind. The bulk velocity and the thermal velocity of the O^{7+} ions are assumed to be similar to those of the solar wind H^+ ions (Hefti et al., 1998).

Finally, from the point of view of the Lorentz force, an O^{7+} ion does not differ significantly from a H^+ ion because the mass per charge ratio, m/q, of O^{7+} ions is $16/7 \sim 2.3$ amu e^{-1}, while it is 1 amu e^{-1} for H^+ ions. In fact, the m/q ratio for O^{7+} ions is close to the m/q ratio of the solar wind He^{++} ions (2 amu e^{-1}) and, consequently, O^{7+} ions are also expected to provide a first-order approximation for the He^{++} ion impact flux regions on the studied surfaces. The role of m/q ratio is investigated in this paper by replacing O^{7+} ions with Fe^{9+} ions which have a larger m/q ratio than O^{7+} ions: $m/q = 56/9 \sim 6.2$ amu e^{-1} for Fe^{9+} ions. The mixing ratio of Fe^{9+} ion was assumed to be identical with that of O^{7+} ions ($n_{SW}(Fe^{9+}) = 7 \times 10^{-4} \times n_{SW}(H^+)$) to help the comparison between the total ion impact flux of the heavy ions. In the actual solar wind the iron fraction is somewhat lower than assumed here, the iron abundance with respect to oxygen is $[Fe/O] = 0.12 \pm 0.03$ and $[Fe/O] = 0.063 \pm 0.007$ for slow and fast solar wind, respectively (Aellig et al., 1999; Wurz et al., 1999). The Fe^{9+} ion is just one of the charge states of iron ions in the solar wind, which range from about Fe^{8+} to Fe^{13+}, with the Fe^{9+} fraction typically being 0.2 for regular solar wind (Aellig et al., 1998). Note that the densities of the oxygen and iron ions in the solar wind are so small compared with the total ion density that they have a negligible effect on the self-consistent solution of the hybrid model calculation and, consequently, the impact rate of the heavy ions depends linearly on the initial density of the solar wind. The derived multiply charged ion impact flux maps can, therefore, also be used to describe other mixing ratios by rescaling the calculated fluxes to the actual mixing ratio. Finally, the velocity of Fe^{9+} and O^{7+} ions were assumed to be identical, which is a good approximation (Hefti et al., 1998), to study the role of the m/q ratio alone.

3. Impacting multiply charged ions

3.1. Overview of the plasma interaction

Fig. 1 shows the density of the solar wind protons near Mercury, the Moon and Ceres based on HYB models. The Moon and Ceres display a similar type of interaction with the solar wind plasma, since the solar wind can freely hit against these objects on the ram side (i.e., at $x > 0$ in the simulation). The density of the solar wind is low on the anti-ram side (i.e., at $x < 0$ in the simulation) and in the case of the Moon a long "cavity" of solar wind ions is formed behind it (see Kallio (2005) for details of the properties of the Lunar tail).

The Hermean intrinsic magnetic field, instead, results in very different plasma environments on both the ram and the anti-ram sides (Fig. 1, top panel). The intrinsic magnetic field of Mercury is strong enough to form a

bow shock, a magnetosphere, a magnetotail, a plasma sheet and a bow shock (see Kallio and Janhunen (2003a, b) for details of the properties of the Hermean magnetosphere in the hybrid model). Panels a and b in Fig. 1 illustrate that Mercury's intrinsic magnetic field is strong enough to prevent the solar wind ions from hitting freely on its surface under nominal solar wind plasma conditions.

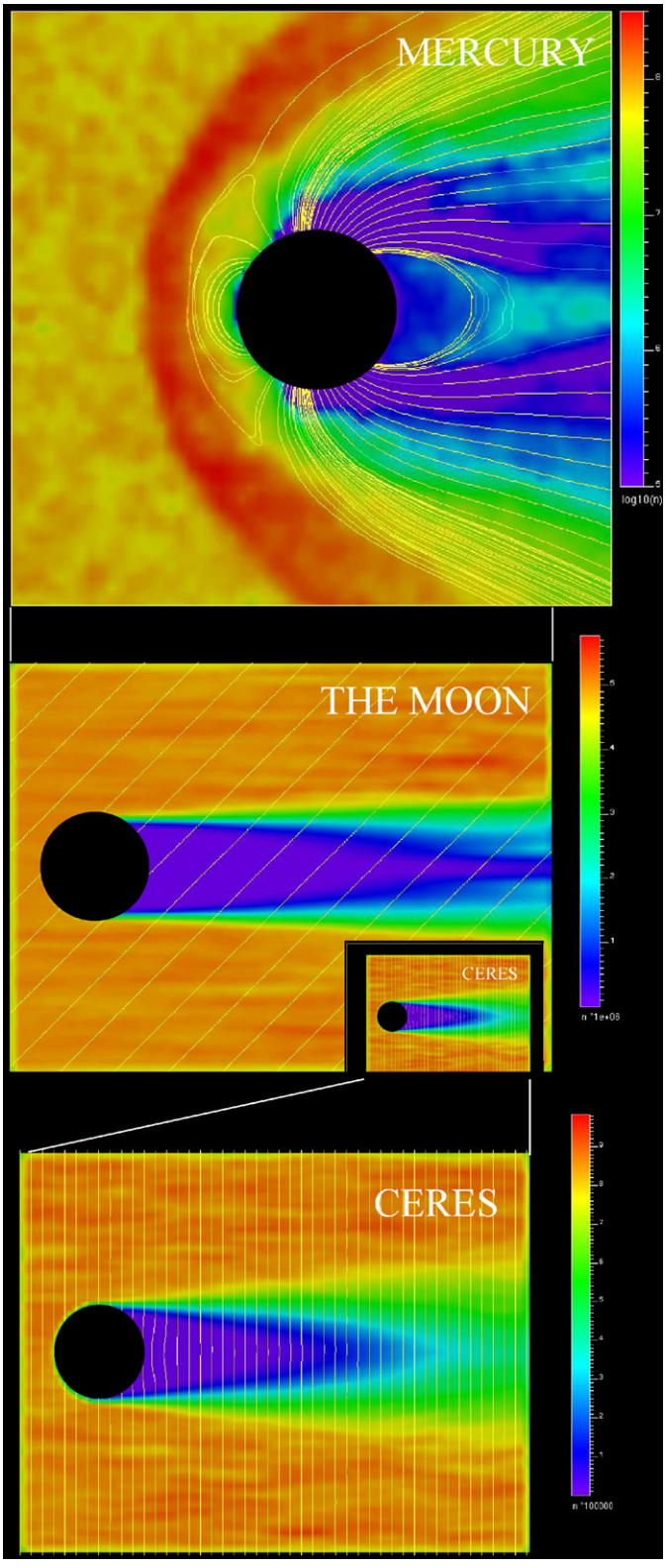

Fig. 2 shows a comparison between the densities of H^+, O^{7+} and Fe^{9+} ions near Mercury in the *xy*-plane, which is the ecliptic plane. In all three cases the ion density was at its minimum behind Mercury. Both in H^+ and O^{7+} ions a clear enhancement in density can be seen at the bow shock. The spatial sizes of the low ion density region (the blue region in Fig. 2) around the planet and behind it are much alike. However, only a very weak enhancement can be seen in $n(Fe^{9+})$ near the bow shock and the size of the low density region is smaller for Fe^{9+} than for H^+ or O^{7+}. Fig. 2, therefore, implies that the macroscopic plasma parameters near Mercury depend both on the undisturbed plasma parameters and on the m/q ratio of ions. Finally, there is a clear dawn ($y<0$) to dusk ($y>0$) asymmetry in that the low-density region extends further to the dusk side than to the dawn side. The dawn–dusk asymmetry can also be seen in the ion impact flux, as will be discussed in detail in Section 3.2.

The motion of individual ions near Mercury was studied (Fig. 3) by launching protons, oxygen and iron ions in the solar wind in the *xz*-plane and in the *xy*-plane. All the test particles were launched with the solar wind velocity in the $-x$-direction and, therefore, the trajectories of these ions in the solar wind were straight lines. The ion gyroradius can be seen at the bow shock where the ions start to have a notable velocity component perpendicular to the *x*-axis, which prevents ions from impacting freely on the surface of Mercury. Gyromotion is hardly seen in the H^+ ion trajectories in Fig. 3 but in O^{7+}, and especially in Fe^{9+} ions, the gyroradius is clearly visible. Only a few of the launched test ions had access to the magnetosphere and that resulted in a low-density tail region that is clearly seen in the ion density plots (cf. Figs. 1 and 2). Note that the dawn–dusk asymmetry is visible both in the O^{7+} and Fe^{9+} trajectories, which were deviated more effectively toward the $-y$-direction than toward the $+y$-direction (panels b, d and f in Fig. 3). This difference is associated with the gradient and curvature drifts that impeled positive ions clockwise when viewed from above the North Pole, as shown in panels b, d and f of Fig. 3. The counterclockwise

Fig. 1. The density of the solar wind protons near Mercury on the *xz*-plane (top panel), near the Moon on the *xy*-plane when it is in the solar wind (middle panel), and near a Ceres-size, non-magnetized and non-atmospheric, asteroid (bottom panel) on the *xy*-plane based on hybrid model calculations. The range of the colour scale is (top) $\log_{10}(n_{SW}(H^+)\ m^{-3}) = [5,\ 8.5]$, (middle) $n_{SW}(H^+) = [0,\ 5.8\cdot10^6]\ m^{-3}$, and (bottom) $n_{SW}(H^+) = [0,\ 9.8\cdot10^5]\ m^{-3}$. In the Mercury model the colour scale is logarithmic while it is linear in the Moon and Ceres plots. Yellow is used to show the magnetic field lines that illustrate that a "mini-magnetosphere" is formed around Mercury in contrast to the Moon and Ceres cases. Note that the spatial size in the Ceres simulation is much smaller that the sizes pertaining in the Mercury and Moon simulations. The small insert in the middle panel shows the Ceres simulation box at the same spatial scale as that used in the Moon and Mercury models. The radii of Mercury, the Moon and Ceres used in the simulations were 2440, 1730 and 470 km, respectively.

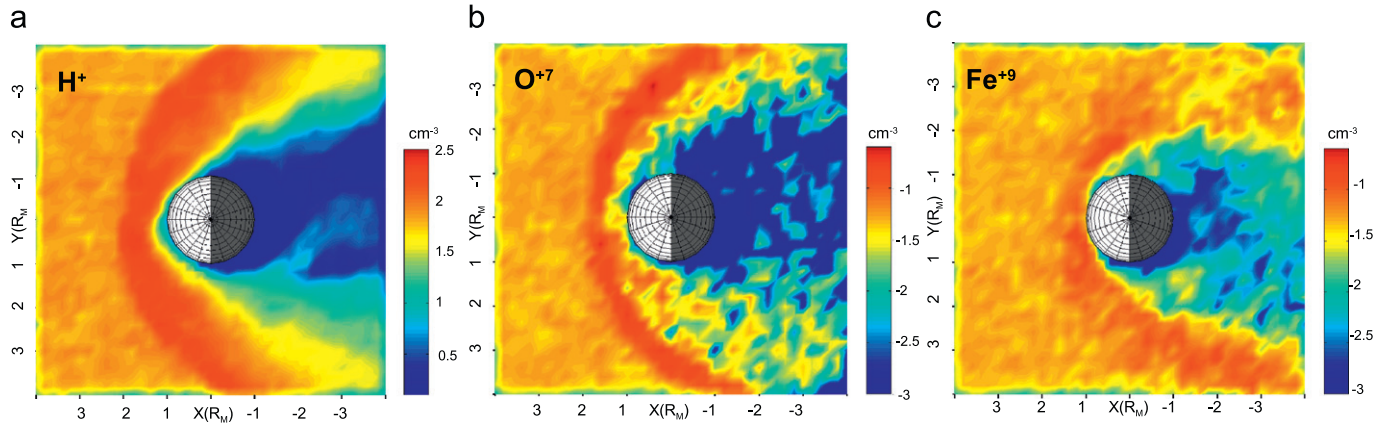

Fig. 2. The density of (a) the solar wind protons, (b) O^{7+} ions and (c) Fe^{9+} ions near Mercury in the *xy*-plane based on a hybrid model calculations. The unit of density is $\log_{10}(n_{SW}(H^+)\,cm^{-3})$. The ion densities in the solar wind were $n_{SW}(H^+) = 6\,cm^{-3}$ and $n_{SW}(O^{7+}) = n_{SW}(Fe^{9+}) = 7\times10^{-4}\times6\,cm^{-3}$. $-y$ corresponds to the dawn side.

drift motions combined with the deviation of the ions around Mercury resulted in a clear dawn–dusk asymmetry for oxygen and iron ions.

3.2. Ion impact fluxes

One important feature illustrated by Fig. 3 is that solar wind ions can impact on the surface of Mercury. It has been shown earlier that, in the case of northward IMF which is analyzed in the present paper, the total ion H^+ impact rate on the surface of Mercury, $q_{tot}(H^+)$, was found to be $\sim3.9\times10^{25}\,s^{-1}$ (Kallio and Janhunen, 2003a, b). Another way to express this result is to calculate the so-called absorption coefficient, c_{abs} ($\equiv q_{tot}/\pi\times R_M^2\times n_{SW}(H^+)\times U_{SW}$), which indicates the percentage of the ions that flow in the undisturbed solar wind through a disk with the radius of a given object so that they impact on the surface of that object. In the case analyzed $c_{abs}(H^+)$ was 0.06, that is, 6%. In the present paper earlier ion impact flux analysis is continued by calculating the ion impact flux mixing ratio between O^{7+} and H^+ ions, $q_{tot}(O^{7+})/q_{tot}(H^+)$, and between Fe^{9+} and H^+ ions, $q_{tot}(Fe^{9+})/q_{tot}(H^+)$. These ratios are then compared with the ion density mixing ratios in the solar wind.

Fig. 4 shows the flux of impacting H^+, O^{7+} and Fe^{9+} ions on the surface of Mercury in the HYB-Mercury model. Note that the statistical fluctuations in the O^{7+} impact map in Fig. 4 are much larger than in the H^+ and Fe^{9+} impact maps because the total number of impacting H^+ ions, O^{7+} ions and Fe^{9+} ions in the simulation are 1.9×10^6, 32×10^3 and 170×10^3, respectively. Because of this difference, a factor of two larger bin sizes in longitude (long.) and latitude (lat.) was used to generate the O^{7+} impact map than was used to produce the H^+ and Fe^{9+} impact maps.

As seen in Fig. 4, all the ion species considered impact on the surface of Mercury non-homogenously. As in a previous hybrid model study (Kallio and Janhunen, 2003a) the highest fluxes in the north IMF case were found to be near the magnetic cusps at long. ~0°, lat. $\sim\pm50°$. However, a comparison between H^+, O^{7+} and Fe^{9+} impact maps implies that the high ion impact flux "spots" are located on the dawn side hemisphere (i.e. long. $<0°$), and that the shifting of the high impact flux spots near noon (long. $=0°$) toward long. $=-90°$ is more pronounced for the high m/q value O^{7+} ions, and especially for the Fe^{9+} ions, that is the case for solar wind protons. This dawn–dusk asymmetry results in a situation where ~56% of O^{7+} ions impact on the dawn side hemisphere. The asymmetry is even stronger for Fe^{9+} ions because ~88% of such ions impact on the dawn hemisphere.

Another clear difference between the ion impact maps presented in Fig. 4 is that the impacting O^{7+} and Fe^{9+} ions do not, in contrast to the impacting H^+ ions, produce high ion impact flux "bands" near the open–closed magnetic field line boundary that is located at lat. $\sim\pm30°$ on the dayside and on the nightside. In fact, the high m/q ratio in the Fe^{9+} case appears to produce a "<" shape in the latitude–longitude ion impact flux map (Fig. 2f), since the high impact flux regions are displaced toward the magnetic equator (lat. $=0°$) with decreasing longitude values when the longitude is between $-180°$ and 0°. Note also that the high O^{7+} and Fe^{9+} impact fluxes reach the magnetic equator on the dusk hemisphere side at long. ~110°, resulting in a local ion impact flux minimum at long. ~[40°, 110°] near the magnetic equator (Fig. 2d and f).

Finally, the ion impact flux mixing ratio $q_{tot}(Fe^{9+})/q_{tot}(H^+)$ is $\sim25\times10^{-4}$, that is more than three times higher than the initial ion mixing ratio of 7×10^{-4} we assumed for in the solar wind. The $q_{tot}(O^{7+})/q_{tot}(H^+)$ ratio is so close to the value 7×10^{-4} that any possible increase in the mixing ration cannot be determined. Note that the estimation of the $q_{tot}(O^{7+})/q_{tot}(H^+)$ ratio cannot be made as accurately as the estimation of the $q_{tot}(Fe^{9+})/q_{tot}(H^+)$, because there is a smaller number of O^{7+} ion hits (32×10^3) than Fe^{9+} ion hits (170×10^3). Although the small number of heavy ion impacts cannot be studied in detail, the correlation between the ion impact flux mixing

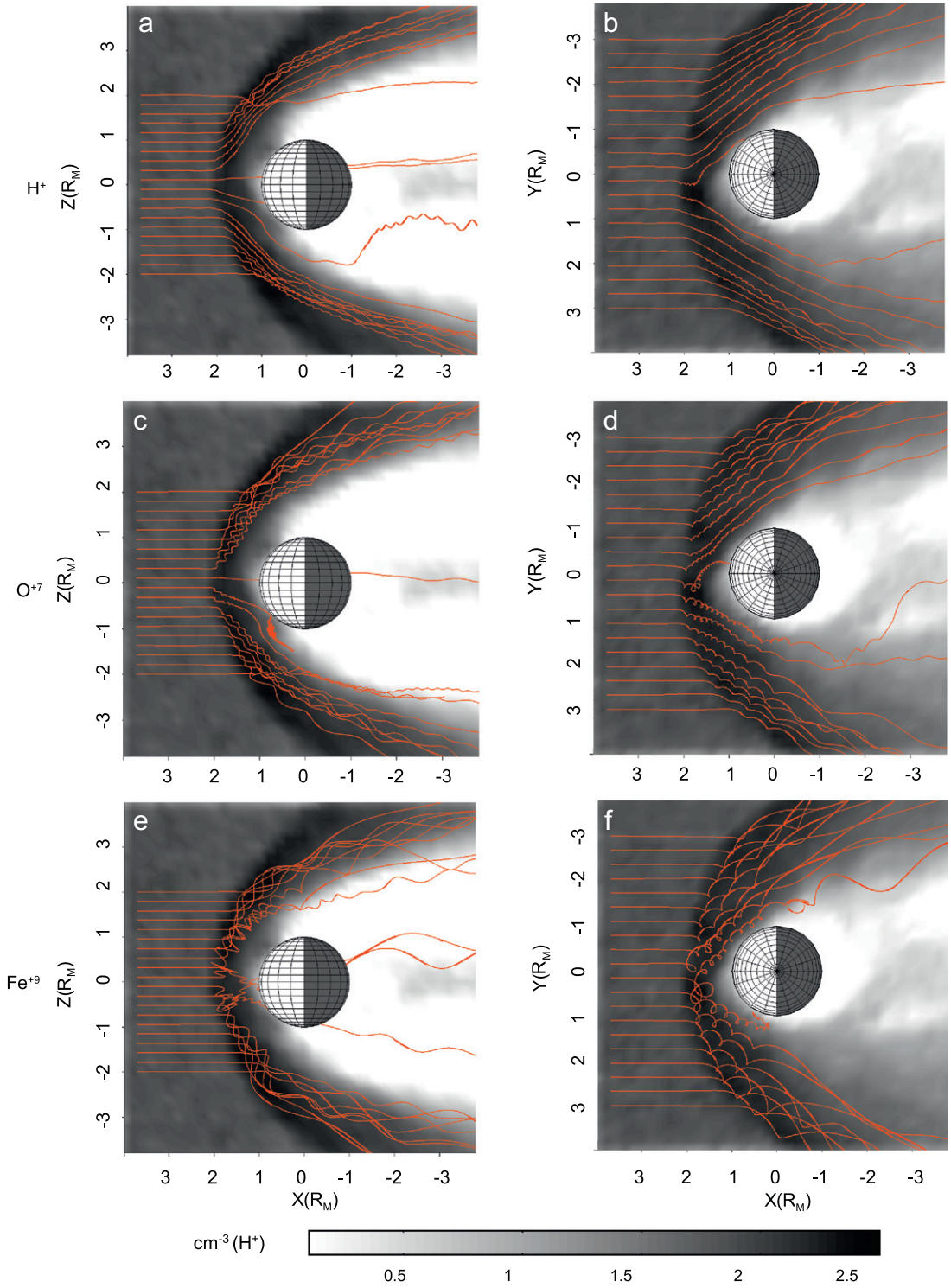

Fig. 3. An illustration of the motion of (panels a and b) H^+ ions, (panels c and d) O^{7+} ions, and (panels e and f) Fe^{9+} ions near Mercury. In panels a, c and e 20 test ions were launched at $x = 3.8R_M$ and $y = 0$ in the region $z = [-2, 2]R_M$ with the solar wind velocity. In panels b, d and f 20 test ions were launched at $x = 3.8R_M$ and $z = 0$ in the region $y = [-3, 3]R_M$. Note that the trajectories (red lines) are in three-dimensional space. The gray scale shows the density of H^+ ions in (panels a, c and e) the xz-plane and (panels b, d and f) in the xy-plane, to depict how the ion trajectories are related to the macroscopic density of the solar wind protons. Note that H^+ ion density planes are shifted to the background so that they do not hide the trajectories.

ratio and the m/q value suggests that solar wind ions with large m/q may transfer more easily to the surface of Mercury. Mercury's intrinsic magnetic field can, therefore, in some sense be deemed to act as an ion mass spectrometer that affects both the spatial distribution of impacting ions on the surface and the total ion impact flux.

Fig. 5 shows the ion impact flux on the Moon where solar wind ions can impact freely on the surface without the

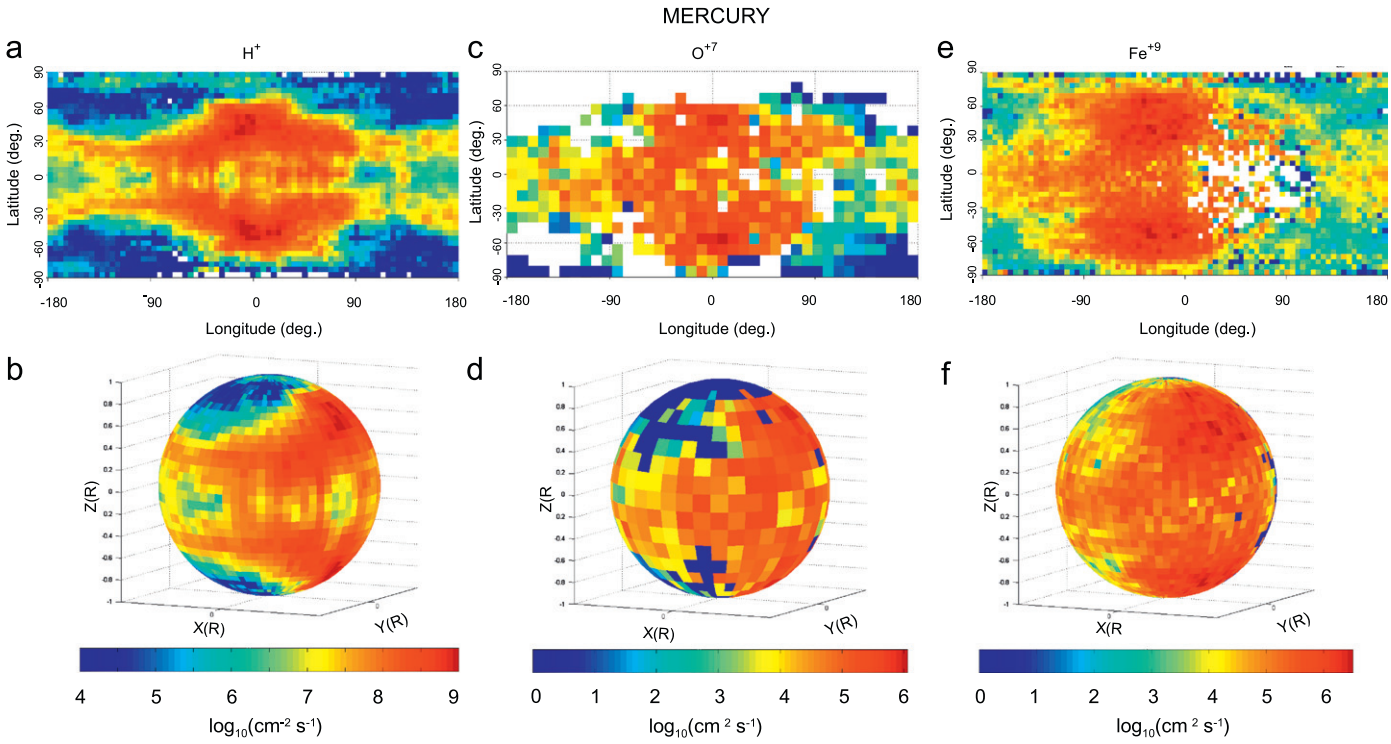

Fig. 4. The particle flux of impacting solar wind (a, b) H^+ ions, (c, d) O^{7+} ions and (e, f) Fe^{9+} on the surface of Mercury. In panels a, c and e the flux of impacting ions are presented in a two-dimensional latitude–longitude map. In that map the sub-ram point is located at lat. = long. = 0°, the dayside is at long. −90° to 90° and the night side is located at long. >90° and at long. <−90°. In panels b, d and f impact maps are shown on the surface of Mercury. In the H^+ and Fe^{9+} maps the bin size is 4.5° × 4.5° in longitude and latitude, and in the O^{7+} map the bin size is 9° × 9°. The colour shows the ion flux in $\log_{10}(cm^{-2}s^{-1})$. The ion densities in the solar wind were $n_{SW}(O^{+7}) = n_{SW}(Fe^{9+}) = 7\times10^{-4}\times n_{SW}(H^+) = 7\times10^{-4}\times 6\,cm^{-3}$ where 7×10^{-4} is the assumed mixing ratio. Note that these impact fluxes can also be used for other mixing ration cases simply by rescaling them by the wanted mixing ratio (see Section 2 for details).

motion of these ions being changed by an intrinsic magnetic field or by collisions with atmospheric particles. In a first-order approximation, the ion impact flux decreases as ~cos(RZA), where RZA is the Ram Zenith Angle: RZA = acos(($\mathbf{U}_{sw}\cdot-\mathbf{r}$)/|$\mathbf{U}_{sw}\cdot\mathbf{r}$|) ($\mathbf{r}$ is a vector from the centre of the object to the analyzed point on the surface). Note that the impact flux is not exactly zero at RZA >90° because of the finite ion gyroradius. The total ion impact flux rates of H^+ ions and O^{7+} ions to the surface of the Moon is 2.5×10^{25} and $1.75\times10^{22}\,s^{-1}$, respectively. The $q_{tot}(O^{7+})/q_{tot}(H^+)$ ratio is 6.98×10^{-4}–7×10^{-4}, which is the same as the density ratio of the ion species assumed for in the solar wind.

Because the non-finite ion gyroradius effects the effective radius of the disk of the absorbing obstacle for H^+ ions, R_{absorb}, is defined as $n_{sw}\times U_{sw}\times\pi\times R^2_{absorb} = q$, where q, the total absorption rate of ions, is slightly larger than the radius of the object: $R_{absorb} = 1757$ km ($= (2.50314\times10^{25}/6\times10^6\times430\times10^3\times\pi)^{1/2}$), that is about 30 km larger than the radius of the Moon (1730 km).

The decrease of the flux as ~cos(RZA) in Fig. 5 indicates also how the ion impact flux depended on RZA in the Ceres-run (figure not shown). The total ion impact flux rate of H^+ ions and O^{7+} ions to the surface of Ceres was 2.6×10^{23} and $1.8\times10^{20}\,s^{-1}$, respectively. The O^{7+}/H^+ impact flux ratio is, therefore, 6.93×10^{-4}–7×10^{-4}, that is about the same as the density ratio of the ion species assumed for in the solar wind.

4. Consequences of the charge exchange processes on the surface

The goal of this paper is to estimate quantitatively the impact rate of multiply charged ions on non-magnetized, or weakly magnetized, Solar System objects (Mercury, the Moon, and Ceres). These impact fluxes are presented in Figs. 4 and 5. The motivation to study such fluxes arises from the fact that the impact of multiply charged ions can result in many physical processes which either cannot occur, or occur much more weakly, when solar wind protons are the impactors.

The impact of solar wind protons on a surface has already been studied using molecular dynamic simulations (see, for example, Nordlund and Averback, 2000) and by means of the commonly used TRIM (the transport of ions in matter) and SRIM (the stopping and range of ions in matter) Monte Carlo models. However, not much is known about the processes which take place when the impacting ion is multiply charged. One of the principal interaction processes, relevant for space science, between a multiply charged ion, say, O^{7+} and target neutrals is CX where O^{7+} captures electrons from a target species X

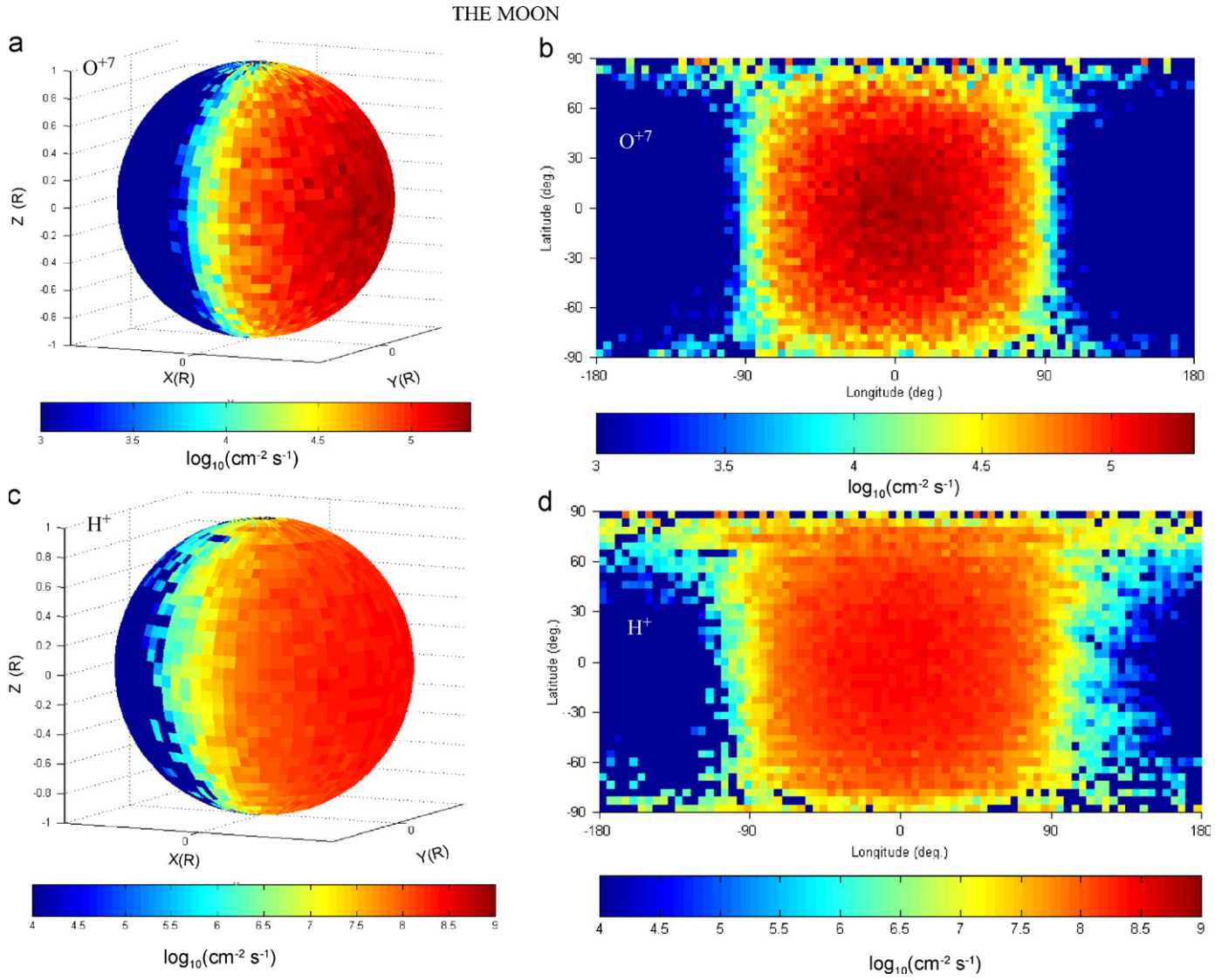

Fig. 5. Particle flux of impacting solar wind (a, b) O^{7+} ions and (c, d) protons on the surface of the Moon, when the Moon is in the solar wind. See Fig. 4 for a description of the ion impact maps.

(e.g. H_2O, O, H, etc.):

$$O^{n+} + X \rightarrow O^{(n-1)+} + X^{1+} + \text{Energy} \quad (1)$$

where n ($n = 7, 6, \ldots, 1$) is the ionization state of the oxygen ion (Fig. 6). Such CX processes in which a multiply charged ion transforms to a lower charge state have received particular attention in cometary research because CX can result in the production of the observed soft X-ray and EUV emissions at comets. During transitions from O^{7+} ions to O atoms the ion emits large numbers of photons at various wavelengths. For example, the total energy emitted by a single exiting oxygen ion at different charge state values for photon energies above 100 eV is 817 eV for O^{7+} ions, 687 eV for O^{6+} and 63 eV for O^{5+} ions (Kharchenko and Dalgarno, 2000). In four capture collisions $O^{7+} \rightarrow O^{4+}$ the total accumulated released energy from the sequential region with energies exceeding 80 eV is 1.65 KeV (Kharchenko and Dalgarno, 2000). That energy is larger than the typical energy of a solar wind proton (~1 keV) but smaller than the typical kinetic energy of the oxygen ion in the solar wind (~16 keV). Moreover, CX processes are anticipated to stimulate soft X-ray emissions in the Martian (Holmström et al., 2001; Holmström and Kallio, 2004) and Venusian (Gunell et al., 2007) exospheres, as well as in the terrestrial magnetosheath (Robertson and Cravens, 2003).

The interaction between multiply and highly charged ions and surfaces is currently under active laboratory research (see extensive review articles by Arnau et al., 1997; Schenkel et al., 1999; Aumayr and Winter, 2003 and references therein). Fig. 7 illustrates several effects associated with heavy ion impact on metallic (Fig. 7a) and insulating (Fig. 7b) surfaces. When a highly charged heavy ion is approaching a metallic or semiconducting surface (e.g. Si or GaAs) it captures electrons, which were pulled out off the surface by the high potential energy of the ion,

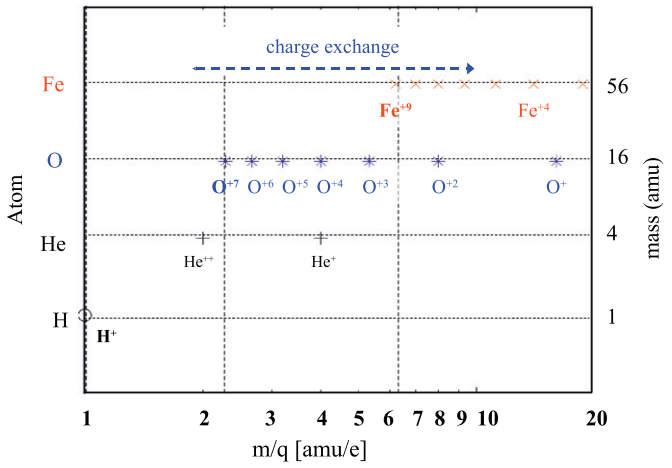

Fig. 6. Charge exchange, ionization state and m/q ratio. In a charge exchange process the ionization state of an ion decreases and, therefore, its m/q ratio increases and the ion moves in Fig. 6 from left to right until it reaches a single charged state. The figure shows three atoms (H, O and Fe) and three m/q ratios (H^+: 1/1; O^{7+}: 16/7; Fe^{9+}: 56/9) analyzed in this paper. Helium (He) is added in the figure to illustrate that the analyzed m/q ratios can also be used to mimic m/q ratios of other atoms (see also the discussion about the Lorentz force in Section 2).

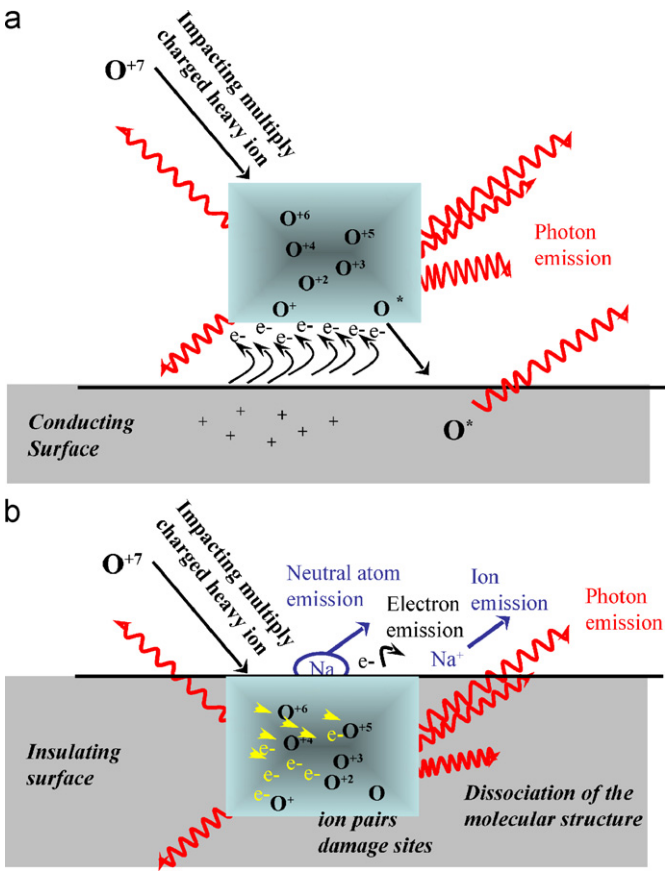

Fig. 7. A schematic illustration of different physical processes which take place when a multiply charged heavy ion, such as solar wind O^{7+} ion, impacts on (a) a metallic and (b) an insulating surface (after Aumayr and Winter, 2003). Such impacts result in the emission of neutrals (say Na), ions (say Na^+), electrons and photons (say X-ray photons) from individual surfaces. See the text for details.

to become a neutral "hollow" atom above that surface (Schenkel et al., 1999; Aumayr and Winter, 2003). Before the multiply charged ion has become fully neutralized it will be accelerated towards the surface by its rapidly decreasing mirror charge, which provides an additional vertical kinetic energy (Burgdörfer et al., 1991; Arnau et al., 1997). Decay of such hollow atoms via auto-ionization and other Auger-type processes is accompanied by electron emissions up to 10 eV. Electron emission and re-neutralization continues until the hollow atom collapses close to the surface. Thus, the multiple charged ion becomes fully neutralized in front of the surface and excited states decay rapidly by autoionization processes described above. But only a fraction of the potential energy which was originally stored in the projectile is released above the surface, while a larger part of the potential energy will be liberated in very close vicinity or even below the surface. When this happens the more tightly bound M, L and K shells have become filled by the Auger neutralization from conduction band or in close collisions with target atoms within the surface (Schippers et al., 1993; Arnau et al., 1997; Aumayr and Winter, 2003). As one consequence X-ray, soft X-ray and EUV photons are produced both above and below the surface when the captured electrons transfer from the outer shells, in which they were captured, to the inner shell vacancies. In solar wind multiply charged ions, as considered in our study, soft X-rays and EUV photons (<1 keV) should be emitted (Schenkel et al., 1999).

Fig. 7b shows a scenario where the surface concerned is an insulator, for example an ionic crystal (e.g. NaCl or LiF). The particle enters the surface as an ion and is, thereafter, neutralized below the surface (Fig. 7b). In insulator-type surfaces the electron mobility is reduced and the sudden modification of the near-surface electronic structure cannot be restored in the short time, therefore potential sputtering and desorption, etc. occur (Aumayr and Winter, 2003). However, for both of these surface-type (conducting/insulating) impact damages the surface. Some of the ions that are released as a result of this interaction, as well as electrons and neutral atoms, can escape from a surface, which are under vacuum. In this way the impacting multiply charged ions may increase the neutral atom, ion and electron density near the surface. Laboratory experiments have shown that there is no increase in the sputtering yield for metallic and for semiconducting surfaces, but the sputter yield can be noticeably increased in the case of a good insulating surface (Aumayr and Winter, 2003). However, having a good insulator is unlikely for a space-weathered planetary surface (Wurz et al., 2007). In any case, the surface will be damaged and space weathering will increase. Since a significant part of the interaction between the multiply charged ion and the surface is via electronic processes the secondary electron yield for a multiply charged ion hitting the surface is large (Arnau et al., 1997), much larger than for protons. In addition, not only the typical low-energy secondary electrons with energies of a few eV are released, but also electrons of much higher

energy from the shell transitions. These electrons may influence the near-planet plasma populations.

As illustrated in Fig. 7b, ion impact on an insulating surface can result in many physical processes that affect both the surface and the space above it. For example, if the emitted soft X-ray or EUV photons can escape from a surface, as discussed above and illustrated in Fig. 7b, then impacting multiply charged heavy ions can be expected to form a non-homogenous X-ray and EUV emission source at the surface of Mercury on both the dayside and the nightside. Also, sputtered neutrals can result in a tenuous exosphere above planetary bodies (e.g. Wurz and Lammer, 2003; Wurz et al., 2007; Killen et al., 2007). Ion impact also affects the properties of overlying plasma by stimulating the emission of ions and electrons.

A detailed study on the efficiency of the various effects (sputter enhancement, electron and soft X-ray and EUV emissions), which are related to multiple charged ion interaction with planetary surfaces, is beyond the scope of this work. However, more laboratory and theoretical studies are called for in the future to estimate quantitatively the role of impacting heavy ions on various objects in the solar system since the properties of the surfaces and the properties of the impacting multiply charged ions (their kinetic energy; the incident angle; the charge state of an ion, e.g. O^{7+}, O^{6+}, O^{5+},…; ion specie: e.g. Fe^{9+}, N^{5+}, Ne^{8+}, etc.) varies from object to object and depends on the activity of the Sun.

In the case we analyzed for Mercury, the IMF was purely northward, resulting in a so-called "closed" magnetosphere. However, in a nominal IMF case at Mercury the x-component of the IMF is the largest magnetic field component. In previous HYB-Mercury model runs (Kallio and Janhunen, 2003a, 2004) the non-zero x-component of the IMF was shown to result in a north–south asymmetry in the H^+ impact flux (see Kallio and Janhunen, 2003a, Fig. 3c). Similar types of asymmetry were also found in previous test particle simulations (Sarantos et al., 2001; Mura et al., 2005). Also, high impact flux "cusp" regions that can be seen in H^+, O^{7+} and Fe^{9+} ions in Fig. 4, suggest that a similar north–south impact flux asymmetry may take place in the case of heavy solar wind ion species. Moreover, a high solar wind density was found to result in high H^+ impact flux all over the dayside hemisphere (see Kallio and Janhunen, 2003a, Figs. 2b and 3d). The question as to whether the same behaviour will be found to characterize heavy solar wind ion impacting fluxes needs to be studied in the future.

5. Summary

We have estimated quantitatively the fluxes of impacting, multiply charged, solar wind ions on the surfaces of Mercury, the Moon and on a Ceres-size asteroid using a hybrid model.

This study demonstrates that the O^{7+} and Fe^{9+} ions analyzed impact the surface of Mercury non-homogenously, controlled by the direction of the Hermean intrinsic magnetic field and by the direction of the interplanetary magnetic field. Especially, O^{7+} and Fe^{9+} ions produce a region characterized by high ion impact flux near the magnetic cusps at Mercury, similar to that produced by impacting solar wind protons. In contrast to solar wind protons, however, these heavy ions do not create a high ion impact flux region near the open–closed magnetic field line boundary. The total impact flux of Fe^{9+} ions on Mercury's surface was found to be larger than the total ion impact flux of O^{7+} ions for the same mixing ratios in the solar wind, indicating that the total ion impact flux of multiply charged ions depends on the mass per charge ratio of the ions.

The ion impact flux on the surface of the non-magnetized Moon and on a Ceres-size asteroid is also non-homogenous, but the flux is axially symmetric with respect to the direction of the solar wind flow and depends only of the angle between the solar wind velocity vector and on the region of the surface analyzed.

Impacting multiply charged heavy ions such as O^{7+} are sources of energy which can result in the generation of ion pairs, electrons and soft X-ray and EUV photons within the surface. The associated energy release may cause the release of ions, electrons, neutrals and photons from the surface, thereby, leading to its non-isotropic space weathering.

References

Aellig, M.R., Grünwaldt, H., Bochsler, P., Wurz, P., Hefti, S., Kallenbach, R., Axford, W.I., Balsiger, H., Bürgi, A., Coplan, M.A., Galvin, A.B., Geiss, J., Gliem, F., Gloeckler, G., Hilchenbach, M., Hovestadt, D., Hsieh, K.C., Ipavich, F.M., Klecker, B., Lee, M.A., Managadze, G.G., Marsch, E., Möbius, E., Neugebauer, M., Reiche, K.-U., Scholer, M., Verigin, M.I., Wilken, B., 1998. Iron freeze-in temperatures measured by SOHO/CELIAS/CTOF. J. Geophys. Res. 103 (A8), 17215–17222.

Aellig, M.R., Hefti, S., Grünwaldt, H., Bochsler, P., Wurz, P., Ipavich, F.M., Hovestadt, D., 1999. The Fe/O elemental abundance ratio in the solar wind as observed with SOHO/CELIAS/CTOF. J. Geophys. Res. 104 (A11), 24769–24780.

Arnau, A., Aumayr, F., Echenique, P.M., Grether, M., Heiland, W., Limburg, J., Morgenstern, R., Roncin, P., Schippers, S., Schuch, R., Stolterfoht, N., Varga, P., Zouros, T.J.M., Winter, H.P., 1997. Interaction of slow multicharged ions with solid surfaces. Surf. Sci. Rep. 27, 113–239.

Aumayr, F., Winter, H., 2003. Potential sputtering. Philos. Trans. R. Soc. Lond. A 1–26.

Bame, S.J., Asbridge, J.R., Feldman, W.C., Kearney, P.D., 1975. Solar wind heavy ion abundances. Sol. Phys. 43, 137–152.

Burgdörfer, J., Lerner, P., Meyer, F.W., 1991. Above-surface neutralization of highly charged ions: the classical over-the-barrier model. Phys. Rev. A 44, 5674–5685.

Cravens, T.E., 1997. Comet hyakutake X-ray source: charge transfer of solar wind heavy ions. Geophys. Res. Lett. 24, 105–108.

Cravens, T.E., 2002. X-ray emission from comets. Science 296 (5570), 1042–1045.

Delcourt, D.C., Moore, T.E., Orsini, S., Millilo, A., Sauvaud, J.-A., 2002. Centrifugal acceleration of ions near Mercury. Geophys. Res. Lett. 29 (12), 1591.

Gunell, H., Kallio, E., Jarvinen, R., Janhunen, P., Holmström, M., Dennerl, K., 2007. Simulations of solar wind charge exchange X-ray emission at Venus. Geophys. Res. Lett. 34, L03107.

Hefti, S., Grünwaldt, H., Ipavich, F.M., Bochsler, P., Hovestadt, D., Aellig, M.R., Hilchenbach, M., Kallenbach, R., Galvin, A.B., Geiss, J., Gliem, F., Gloeckler, G., Klecker, B., Marsch, E., Möbius, E., Neugebauer, M., Wurz, P., 1998. Kinetic properties of solar wind minor ions and protons measured with SOHO/CELIAS. J. Geophys. Res. 103 (A12), 29697–29704.

Holmström, M., Kallio, E., 2004. The solar wind interaction with Venus and Mars: energetic neutral atom and X-ray imaging. Adv. Space Res. 33 (2), 187–193.

Holmström, M., Barabash, S., Kallio, E., 2001. X-ray imaging of the solar wind–Mars interaction. Geophys. Res. Lett. 28, 1287–1290.

Kallio, E., 2005. Formation of the lunar wake in quasi-neutral hybrid model. Geophys. Res. Lett. 15 (32), L06107.

Kallio, E., Janhunen, P., 2003a. Solar wind and magnetospheric ion impact on Mercury's surface. Geophys. Res. Lett. 30 (17), 1877.

Kallio, E., Janhunen, P., 2003b. Modelling the solar wind interaction with Mercury by a quasineutral hybrid model. Ann. Geophys. 21 (11), 2133–2145.

Kallio, E., Janhunen, P., 2004. The response of the Hermean magnetosphere to the interplanetary magnetic field. Adv. Space Res. 33 (12), 2176–2181.

Kharchenko, V., Dalgarno, A., 2000. Spectra of cometary X-rays induced by solar wind ions. J. Geophys. Res. 105 (A8), 18351–18359.

Killen, R.M., Ip, W.-H., 1999. The surface-bounded atmosphere of Mercury and the Moon. Rev. Geophys. 37, 361–406.

Killen, R.M., Potter, A.E., Reiff, P., Sarantos, M., Jackson, B.V., Hick, P., Giles, B., 2001. Evidence for space weather at Mercury. J. Geophys. Res. 106 (E9), 20509–20525, (2000JE001401).

Killen, R., Cremonese, G., Lammer, H., Orsini, S., Potter, A.E., Sprague, A.L., Wurz, P., Khodachenko, M.L., Lichtenegger, H.I.M., Milillo, A., Mura, A., 2007. Processes that promote and deplete the exosphere of Mercury. Space Sci. Rev. 132, 251–328.

Massetti, S., Orsini, S., Milillo, A., Mura, A., De Angelis, E., Lammer, H., Wurz, P., 2003. Mapping of the cusp plasma precipitation on the surface of Mercury. Icarus 166, 229–237.

Milillo, P., Wurz, S., Orsini, A., Delcourt, D., Kallio, E., Killen, R.M., Lammer, H., Massetti, S., Mura, A., Barabash, S., Cremonese, G., Daglis, I.A., De Angelis, E., Di Lellis, A.M., Livi, S., Mangano, V., Torkar, K., 2005. Surface-exosphere-magnetosphere system of Mercury. Space Sci. Rev. 117 (3–4), 397–443.

Mura, A., Orsini, S., Milillo, A., Delcourt, D., Massetti, S., De Angelis, E., 2005. Dayside H^+ circulation at Mercury and neutral particle emission. Icarus 175 (175), 305–319.

Nordlund, K., Averback, R.S., 2000. Collision cascades in metals and semiconductors: defect creation and interface behaviour. J. Nucl. Mater. 276, 194–201.

Robertson, I.P., Cravens, T.E., 2003. X-ray emission from the terrestrial magnetosheath. Geophys. Res. Lett. 30 (8).

Sarantos, M., Reiff, P.H., Hill, T.W., Killen, R.M., Urquhart, A.L., 2001. A Bx-interconnected magnetosphere model for Mercury. Planet. Space Sci. 49, 1629–1635.

Sarantos, M., Killen, R.M., Kim, D., 2007. Predicting the long-term solar wind ion sputtering source at Mercury. Planet. Space Sci. 55 (11), 1584–1595.

Schenkel, T., Hamza, A.V., Barnes, A.V., Schneider, D.H., 1999. Interaction of slow, very highly charged ions with surfaces. Prog. Surf. Sci. 61, 23–84.

Schippers, S., Hustedt, S., Heiland, W., Köhrbrück, R., Bleck-Neuhaus, J., Kemmler, J., Lecler, D., Stolterfoht, N., 1993. Deexcitation of hollow atoms—autoionization of multiply excited N, O, and Ne atoms at a Pt (1 1 0) surface. Nucl. Instrum. Methods Phys. Res. B 78, 106–112.

Shemansky, D.E., 2003. The role of solar wind heavy ions in the space environment. In: Rarefied Gas Dynamics: 23rd International Symposium. AIP Conference Proceedings, vol. 663, pp. 687–695, 10.1063/1.1581610.

Von Steiger, R., Schwadron, N.A., Fisk, L.A., Geiss, J., Gloeckler, G., Hefti, S., Wilken, B., Schweingruber-Wimmer, R.F., Zurbuchen, T.H., 2000. Composition of quasi-stationary solar wind flows from Ulysses/solar wind composition spectrometer. J. Geophys. Res. 105, 27217–27238.

Wurz, P., Lammer, H., 2003. Monte-Carlo simulation of Mercury's exosphere. Icarus 164 (1), 1–13.

Wurz, P., Aellig, M.R., Bochsler, P., Hefti, S., Ipavich, F.M., Galvin, A.B., Grünwaldt, H., Hilchenbach, M., Gliem, F., Hovestadt, D., 1999. The iron, silicon, and oxygen abundance in the solar wind measured with SOHO/CELIAS/MTOF. Phys. Chem. Earth (C) 24 (4), 421–426.

Wurz, P., Rohner, U., Whitby, J.A., Kolb, C., Lammer, H., Dobnikar, P., Martín-Fernández, J.A., 2007. The lunar exosphere: the sputtering contribution. Icarus 191, 486–496.